nanomaterials

MDPI

Article

Reduced Potential Barrier of Sodium-Substituted Disordered Rocksalt Cathode for Oxygen Evolution Electrocatalysts

Aditya Narayan Singh [1], Amir Hajibabaei [2], Miran Ha [2], Abhishek Meena [3], Hyun-Seok Kim [4], Chinna Bathula [4,*] and Kyung-Wan Nam [1,5,*]

[1] Department of Energy and Materials Engineering, Dongguk University-Seoul, Seoul 04620, Republic of Korea
[2] Center for Superfunctional Materials, Department of Chemistry, Ulsan National Institute of Science and Technology (UNIST), 50, UNIST-gil, Ulsan 44919, Republic of Korea
[3] Division of Physics and Semiconductor Science, Dongguk University-Seoul, Seoul 04620, Republic of Korea
[4] Division of Electronics and Electrical Engineering, Dongguk University-Seoul, Seoul 04620, Republic of Korea
[5] Center for Next Generation Energy and Electronic Materials, Dongguk University-Seoul, Seoul 04620, Republic of Korea
* Correspondence: cdbathula@dongguk.edu (C.B.); knam@dongguk.edu (K.-W.N.)

Abstract: Cation-disordered rocksalt (DRX) cathodes have been viewed as next-generation high-energy density materials surpassing conventional layered cathodes for lithium-ion battery (LIB) technology. Utilizing the opportunity of a better cation mixing facility in DRX, we synthesize Na-doped DRX as an efficient electrocatalyst toward oxygen evolution reaction (OER). This novel OER electrocatalyst generates a current density of 10 mA cm^{-2} at an overpotential (η) of 270 mV, Tafel slope of 67.5 mV dec^{-1}, and long-term stability >5.5 days' superior to benchmark IrO_2 (η = 330 mV with Tafel slope = 74.8 mV dec^{-1}). This superior electrochemical behavior is well supported by experiment and sparse Gaussian process potential (SGPP) machine learning-based search for minimum energy structure. Moreover, as oxygen binding energy (O_{BE}) on the surface closely relates to OER activity, our density functional theory (DFT) calculations reveal that Na-doping assists in facile O_2 evolution (O_{BE} = 5.45 eV) compared with pristine-DRX (6.51 eV).

Keywords: cation disordered rocksalt; oxygen evolution reaction; sparse Gaussian process potential; machine learning; density functional theory

Citation: Singh, A.N.; Hajibabaei, A.; Ha, M.; Meena, A.; Kim, H.-S.; Bathula, C.; Nam, K.-W. Reduced Potential Barrier of Sodium-Substituted Disordered Rocksalt Cathode for Oxygen Evolution Electrocatalysts. *Nanomaterials* **2023**, *13*, 10. https://doi.org/10.3390/nano13010010

Academic Editor: Rosario Pereiro

Received: 5 December 2022
Revised: 15 December 2022
Accepted: 16 December 2022
Published: 20 December 2022

1. Introduction

As our reliance on eco-friendly and renewable energy grows, there is an urgent need to explore various sustainable sources. In this race, solar energy is considered an enormous energy source that can permanently solve the world's energy crisis [1,2]. However, a few hours of sunshine in a day, uneven power density distribution on the earth due to geographical area, and low power conversion efficiencies of photovoltaic devices threaten its widespread acceptability [3,4]. Of several other renewable energy resources, the splitting of water to generate hydrogen as a fuel and oxygen as a byproduct is the most viable technique. However, in several electrochemical reactions, the energy conversion rate and efficiency are often limited by oxygen evolution reaction (OER) expressed as equation (1) in aqueous media [5]. This reaction proceeds via multiple-state reactions involving 4 electron oxidations, thus, becoming kinetically sluggish. The η needs to be lowered to accelerate this reaction kinetically. Therefore, several OER electrocatalysts exhibiting lower η have been explored so far [6–8].

$$4OH^- \rightarrow 2H_2O + 4e^- + O_2\ ;\ E = 1.23\ V\ versus\ RHE \quad (1)$$

Over the past few decades, numerous 3d transition metal (TM)-based layered oxide cathodes have been explored to act as OER catalysts [6–10]. It has also been reported that the properties of a Co-based, efficient OER electrocatalyst, particularly Co_3O_4 [11], can be effectively tuned up by lithium insertion/deinsertion as in $LiCoO_2$ [7]. Apart from a single 3d TM containing OER electrocatalysts, a dual 3d TM Fe-substituted $LiNiO_2$ has also been reported to be an efficient electrocatalyst [8]. The higher activity of this doubly doped layered oxide is attributed to the higher oxidation states of TMs and their stabilization in layered structures [12]. So far, several layered oxides have only been looked upon as a suitable host for stabilizing the highly oxidized TM species necessary for effective OER catalysis. Though layered oxides are better suited to stabilize oxidized TM species, it has also been predicted that the electronic state regulation is another avenue to enhance the activity of perovskite electrocatalysts [13]. In this realm, doping is an effective strategy to tailor the oxidation states of TM ions in layered oxides, to effectively promote hole hopping between TM^n to $TM^{(n+1)}$ ions [14,15]. However, the binding energy (BE) of surface oxygen is another vital aspect in OER catalysis, which has rarely been considered in previous reports. Thus, the study must be taken up to understand the role of BE of TMs with surface oxygen in the presence of doped cations/anions.

Herein we report, for the very first time, a uniquely combined 3d/4d TMs-based cation-disordered rocksalt (DRX) cathode [16] material with Na-substitution in the lattice framework by the facile solid-state route. This uniquely combined 3d/4d TMs DRX cathode is believed to entirely change the stacking sequence to that of just 3d TMs cathode while doping of monovalent cation substitution assists in promoting the oxidation state of TMs. The X-ray diffraction and other characterization techniques reveal that Na-substitution significantly assists in OER. The Na-substituted disordered cathode achieves a small Tafel slope of 67.5 mV dec^{-1}, η of 270 mV at a current density of 10 mA cm^{-2}, better than that of the IrO_2 benchmark catalyst, and long-term stability over 133 h. The machine learning aid to search for the minimum energy structure along with density functional theory (DFT) calculations reveals that the oxygen BE is ~6.51 eV in pristine. In comparison, it is much lower (~5.45 eV) in Na-substituted cathode. The higher activity in the Na-substituted DRX cathode is attributed to the facile desorption of O_2 from the surface (Scheme 1).

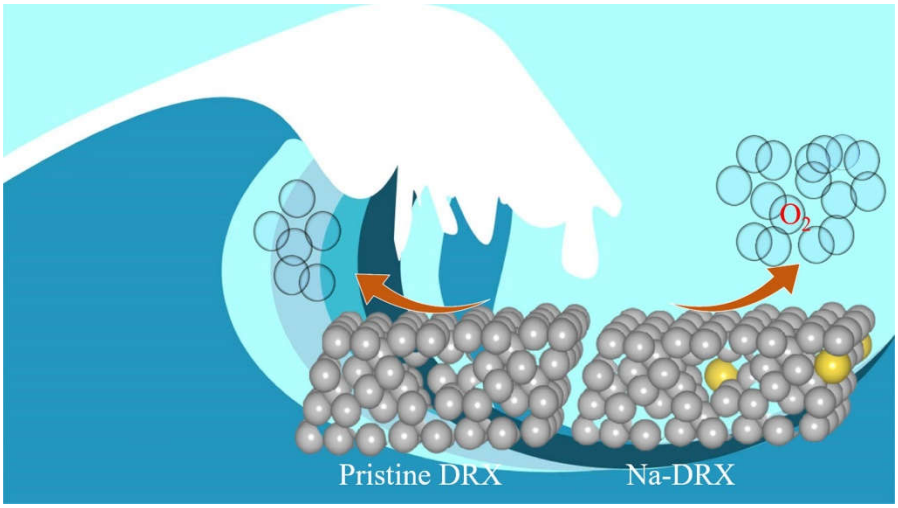

Scheme 1. Schematic illustration of facile O_2 desorption from the surface.

2. Experimental Section

2.1. Materials and Reagents

Lithium nitrate (7790-69-4) and Ru (IV) oxide anhydrous (12036-10-1) were purchased from Acros Organics (Fair Lawn, New Jersey, USA). Sodium nitrate (7631-99-4) and nickel acetate tetrahydrate (6018-89-9) were purchased from Sigma-Aldrich (St. Louis, Missouri, USA). Acetone was purchased from Samchun Chemicals (Gangnam-gu, Seoul, South Korea).

2.2. Syntheses of Disordered Cathode Active Material

We opted for a conventional solid-state reaction method with a slight modification to synthesize cathode active materials calcined at 950 °C. DRX cathode materials, precisely $Li_{1.22}Ru_{0.61}Ni_{0.16}O_2$ (**1**) and $Li_{1.22}Ru_{0.61}Na_{0.05}Ni_{0.10}O_2$ (**2**) were synthesized. The powders of $LiNO_3$, $NaNO_3$, $Ni(CH_3COO)_2.4H_2O$, and RuO_2 were stoichiometrically calculated and thoroughly homogenized using mortar and pestle for around 10 min. Subsequently, the powders were mixed with acetone, followed by ball milling for the next four hours. To compensate the loss during high-temperature synthesis, an excess of 5 wt% of $LiNO_3$ and $NaNO_3$ was taken. The homogenized mixture was then dried overnight in a vacuum oven at 100 °C. The powders were again mortar-pestled, and finally, powders were transferred in an alumina crucible for sintering at 950 °C for 12 h at a ramp rate of 5 °C/min in a tube furnace in the ambient atmosphere. Subsequently, the furnace was cooled to room temperature, and samples were ground manually to obtain a fine powder.

2.3. Materials Characterization

To identify the crystal structures, high-power powder X-ray diffraction (HP-PXRD) data were obtained on a Rigaku X-ray diffractometer (3 phase, 380 V, 18 kW) equipped with Cu Kα radiation (λ = 1.54 Å) in the 2θ range of 10–80°. The XRD samples were prepared by depositing a thick film of cathode powder on a glass substrate. To reveal the morphology and chemical composition of samples, a JEM-2200FS (Cs corrected STEM) HRTEM coupled with an energy-dispersive X-ray spectrometer (EDX, Oxford-INCA) at an acceleration voltage of 200 kV was used. Samples for the HRTEM analysis were prepared following a conventional standard procedure by dispersing in ethanol and then sonicating for a while. The well-dispersed suspension was dropped on TEM Cu-grid and oven-dried to use for HRTEM analysis.

2.4. ICP-OES

Inductively coupled plasma optical emission spectrometry (ICP-OES) was used to determine the exact stoichiometry of the synthesized cathodes.

2.5. XPS data collection and analysis

X-ray photoelectron spectroscopy (XPS) data were obtained on K-alpha (thermo fisher, Brighton, UK). The XPS data were analyzed using the commonly known XPS peak fitting software CasaXPS version 2.3.22.

2.6. OER

The electrochemical characterizations involved in our study were carried out with a three-electrode system on VSP (BioLogic Science Instruments, Inc., Seyssinet-Pariset, France) with a graphitic rod and a calibrated Hg/HgO (Figure S8) as a counter and reference electrode, respectively. Nickel foam (NF) was engaged as a working electrode. Through a drop-casting method on NF, a 1 mg cm^{-2} loading amount of the catalysts was achieved for all working electrodes. To ensure that experiments are conducted under equilibrium conditions of H_2O/O_2, the electrolyte (1M KOH) was continuously kept in flowing oxygen environments for at least 20 min. The linear sweep voltammograms test was performed at a scan rate of 2 mV s^{-1} with 95% iR compensation. Chronopotentiometry

at fix current density of 10 mA cm^{-2} is used to evaluate the long-term stability of the catalyst. The measured voltage values were converted to the reversible hydrogen electrode (R.H.E.) using the following equation: $E_{RHE} = E_{\mathrm{Hg/HgO}} + E^{0}_{\mathrm{Hg/HgO}} + 0.059\times\mathrm{pH}$. Tafel slopes were obtained from $\eta = b \log j + C$; (where η, b, j, and C represent overpotential, Tafel slope, current density, and intercept, respectively). Finally, the overpotential value was obtained by η = E vs (R.H.E) − 1.23.

2.7. DFT Calculations

The Vienna Ab initio Simulation Package (VASP) [17], which implements the projector augmented-wave [18] approach to DFT with PBE GGA functionals [19], is used for all FP calculations. Calculations are spin-polarized, and a kinetic energy cutoff of 500 eV is applied. Due to the large size of unit cells, the Γ-centered k-Point grid of (1,2,3) is chosen. (U; J) values of (4:5; 0:6) for Ru and (4:7; 1:0) for Ni are utilized for PBE+U calculations. A huge number of potential energy calculations were needed to find the favorable doping positions and the minimum energy structures. A machine learning potential is built on-the-fly for accelerating the structure search with a sparse Gaussian process potential (SGPP) algorithm [20–22] as implemented in the AutoForce package.

2.8. Genetic Algorithm

After obtaining the unit-cell formula consistent with doping, we searched for the minimum energy structure by switching the relevant atomic positions. A variation of the genetic algorithm (GA) is used. The search starts with a few random parent structures. At each step, tens of children are generated randomly for each parent. Dozens of lowest energy structures among the union of parents and the new generation are kept as parents for the next generation. The search is stopped if the parents set stays mostly the same for a few steps. Several independent investigations are carried out. The search is accelerated with an SGPP machine learning model, which is built on-the-fly. If the ML model is estimated to be inadequate at every energy calculation step, exact DFT calculations are carried out, and the model is updated.

3. Results and Discussion

A solid-state synthesis route was used to obtain DRX $Li_{1.22}Ru_{0.61}Ni_{0.16}O_2$ and $Li_{1.22}Ru_{0.61}Na_{0.05}Ni_{0.10}O_2$, hereafter denoted as **1** and **2**, respectively. The bulk composition was determined using inductively coupled plasma optical emission spectroscopy (ICP-OES), closely following the theoretical composition (Table S1 and Experimental Section). The crystal structure determined using high-power powder X-ray diffraction (HP-PXRD) reveals that the most characteristic XRD peaks (Figure 1a) in both cathodes are assigned to the C2/c space group of Li_2RuO_3 [23,24]. The merged peaks ~63° indicate disordered structures of the synthesized cathodes [25]. Compared to **1**, the XRD patterns of **2** show the asymmetric peak broadening effect (marked by the green circle in Figure 1a), a signature of lattice defects/strains/dislocation [26] possibly arising from slightly larger radii of Na^+ doped in Li slab. These defects reflected in the form of peak broadening in the XRD pattern confirm that Na^+ is uniformly distributed inside the layered lattice of **2**. The previous report suggests that doping-induced lattice defects are expected to enhance electrochemical performances [27]. To elucidate the electronic structures, the core-level XPS data were obtained. The XPS peak fitting data (Figure 1b and Supplementary Discussion S1) reveal that Na^+ doping brought significant changes in electronic structure. Before moving to the discussion of XPS peak fitting, we disclose the BE of Na. The BE value of ~1071.38 eV (Figure 1c) corresponds to the Na^+ states of Na, indicating that Na has been electro-positively doped in the crystal framework. The Ni 2p (Figures 1d and S1a) possesses two spin-orbit doublets at 855.28 (Ni $2p_{3/2}$) and 872.48 eV (Ni $2p_{1/2}$) accompanied by two satellites at 861.28 and 879.68 eV. The BE ~855.28 eV corresponds to Ni^{3+}, whereas deconvolution of Ni $2p_{1/2}$ reveals two sets of energy bands: 872.48 eV and

873.88 eV for OH^-/OOH. This XPS revelation of Ni hints toward the presence of more Ni^{3+} species favoring the electrophilicity of adsorbed O, thereby catalyzing the formation of -OOH species from OH^- (these steps are considered as rate-determining steps in alkaline media) [4,28]. The electronic structure of Ru in **2** is also different from **1** (Figure S1b). The Ru $3d_{5/2}$ can only be fitted with a doublet (separated by ~1 eV), indicating the presence of both metallic (280.68 eV) and oxidized ruthenium on the surface (Figure 1e). This oxidized ruthenium can be inferred as oxides with low BE (281.98 eV) and with high BE (283.78 eV) [29]. The BEs at 285.38 and 286.68 eV correspond to RuO_x/Ru. Most importantly, XPS results of the O 1s core-level (Figure 1f), fitted with three components apportioned as oxidative oxygen (O_2^{2-}/O^-: BE ~529.58 eV), carbonate/hydroxides/oxyhydroxides species (CO_3^{2-}/OH^-/OOH: BE ~531.48 eV), and absorbed water (H_2O: BE ~534.88 eV) suggest a relatively more significant number of O_2^{2-}/O− species in **2**. This indicates a surplus amount of surface oxygen vacancies [30] compared to **1** (Figure S1c) with hydroxides (BE ~531.7 eV) and oxygen species (BE ~533.4 eV). Firstly, Na doping has significantly modified the electronic structure, which agrees with previous reports on layered cathodes [6,8]. Secondly, the excess of O_2^{2-}/O− species on the surface of **2** is beneficial for catalyzing OER reactions in alkaline media [31,32].

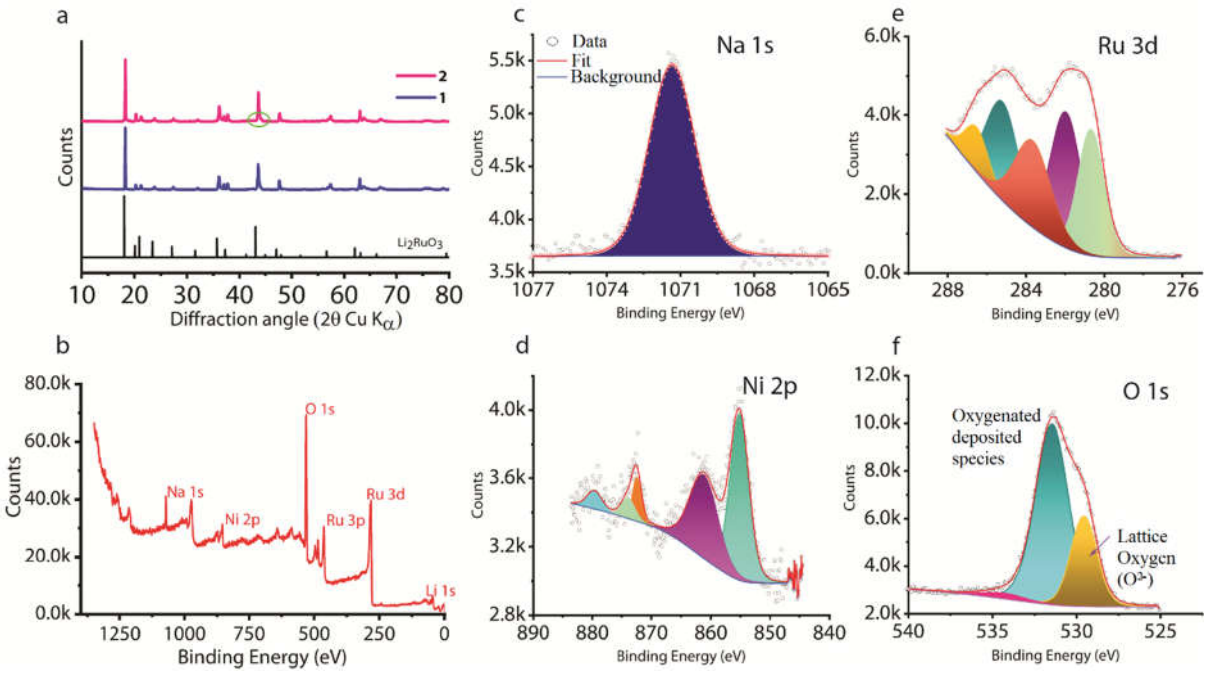

Figure 1. Bulk and surface characterizations. (**a**) HP-PXRD diffraction pattern of **1** and **2**. The peaks are indexed to Li_2RuO_3. (**b**) The core-level XPS survey spectrum. The XPS core-level spectra of constituent elements in **2**: (**c**) Na 1s. (**d**) Ni 2p. (**e**) Ru 3d. (**f**) O 1s. The Li_2RuO_3 cif [mp-4630] was collected from the Materials Project data repository. The Ru $3d_{5/2}$ doublets (BE = 280.68 and 281.98 eV) indicate metallic Ru and RuO_2, respectively.

Scanning electron microscopy (SEM) images reveal a distinguishable feature in their morphology (Figure 2a and Supplementary Discussion S2). The particles in **2** show cornered-shaped structures with smaller particles decorating larger particles, thus, creating rougher surfaces. These rough surfaces expose multiple active sites facilitating oxygen evolution reactions [33]. A better sintering ability with enhanced particle connectivity is an additional feature achieved by Na doping. The lattice fringe distance of 0.475 nm revealed under high-resolution transmission electron microscopy (HRTEM) image corresponds to the disordered structure (Figure 2b). As expected, Na^+ (marked by the pink arrow) distributes uniformly inside the lattice (Figure 2c). Other interesting features that promote OER kinetics can be explored under HRTEM. For instance, defective

zones (marked by the yellow arrow) can also be seen in Figure 2c of Na-DRX, whereas no such beneficial features can be seen in **1** (Figure S2**)**. These defective zones are termed as stacking fault defects, primarily arising from the differences in ionic radii of Na^+ and Li^+ [34,35]. These defective sites can modulate the electronic structure and tune surface properties of **2**, thus, optimizing the adsorption energies of OER steps [27,36]. The autocorrelated image reveals the Na-doping and defects zone (Figure 2d). The energy-dispersive X-ray spectroscopy (EDS) mapping images show a uniform distribution of elements with a slight increase in elemental O on the surface.

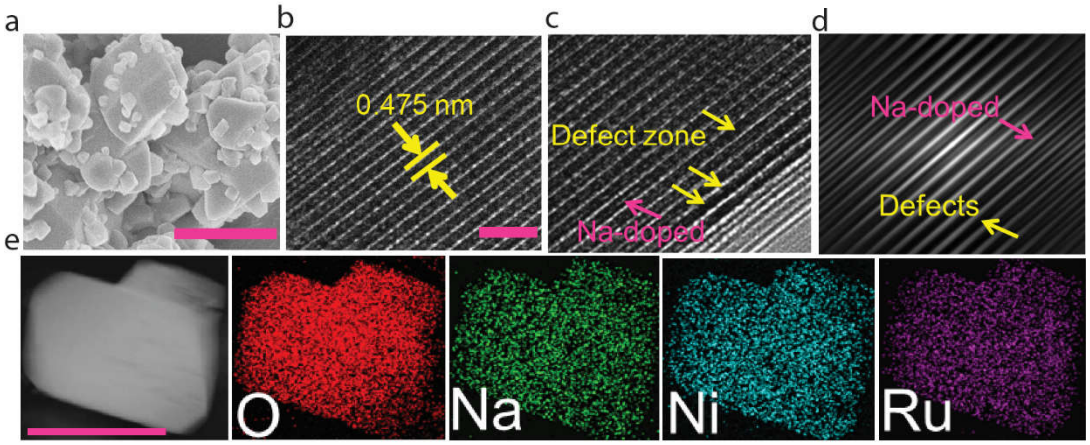

Figure 2. Morphological and structural characterizations. (**a**) SEM image of **2** showing several small particles decorating larger particles (scale bar 2 μm). (**b**) Representative HRTEM image showing lattice fringe distance 0.475 nm corresponding to (002). (scale bar 2 nm). (**c**) HRTEM image showing defective zones (marked with yellow color) and the lattice Na-doped (marked with pink color). (**d**) the autocorrelated image corresponding to c. (**e**) High-angle annular dark-field scanning transmission electron microscopy (HAADF-STEM) and EDS elemental mapping showing the uniform distribution of elements with a slightly increased concentration of elemental oxygen on the surface of **2** (scale bar 250 nm).

To further corroborate the increased oxygen vacancies through Na-doping, the electrochemical oxygen intercalation in **1** and **2** was probed through cyclic voltammetry (CV) performed on a three-electrode system in oxygen saturated 1M KOH electrolyte environment. As illustrated in Figure 3a, redox peaks appear as oxygen ions are inserted into and extracted from the accessible lattice vacancy sites. It is important to note that **2** shows positive-shifted redox peaks (marked by arrows) compared to **1**, which is in harmony with the increased BE reflected by XPS. Furthermore, the linear sweep voltammetry (LSV) curve of **2** exhibits a low η of 270/390 mV (on NF) to yield current densities of 10/250 mA cm^{-2} (Figures 3b and S3a). This catalytic activity is much better than **1** and several other cathode materials deployed for water catalysis (Table S2). As the reaction kinetics directly relates to the electrochemically active surface area, we also evaluated double-layer capacitance (C_{dl}) measurements to compare the electrochemically active surface areas of **1** and **2** (Figures S3b–S5). The double-layer capacitance **2** (C_{dl} = 1.63 mF cm^{-2}) is higher than **1** (C_{dl} = 1.25 mF cm^{-2}), which suggests that the former possesses a relatively higher density of active sites for catalytic reactions, thus, further boosting the OER activities.

To get better insights into OER kinetics, the Tafel slopes of the cathodes were obtained from the steady-state polarization curve. Figure 3c manifests that the Tafel slope of **2** (67.5 mV dec^{-1}) is lower than **1** (72.2 mV dec^{-1}) and benchmark IrO_2 (86 mV dec^{-1}) [8]. The lower Tafel slope value of **2** indicates that the Na^+ substitution into the DRX matrix plays a vital role in promoting the electrochemical OER kinetics, thus, improving the intrinsic catalytic activity.

To evaluate the impact of Na^+ doping on electrical conductivity in **2**, we studied its impedance spectra (Figures 3d and S6). The semicircle is related to the charge-transfer resistance (R_{ct}) of the cathode materials. The electrochemical impedance spectroscopy (EIS) spectra show that the charge-transfer resistance of **2** (R_{ct} = 16.01 Ω) is lower than **1** (R_{ct} = 20.89 Ω) and much lower than the commercial IrO_2 (72.8 Ω), indicating a better electron transfer capability across the electrode/electrolyte interface, thereby indicating a superior OER kinetics and an improved overall electrochemical performance (Figure 3e).

The long-term stability of cathode materials is another crucial factor that deters the wide applicability of DRX materials for water-splitting reactions. We, therefore, investigated the stability in 1M KOH. The chronopotentiometry results suggest that **2** has superb stability of more than 5.5 days and even beyond without an appreciable increment in overpotential (Figures 3f and S7). In contrast, **1** shows a tendency to increase in potential even after a few hours. This superb stability of **2** is attributed to the following factors. The Na doping in the lattice increased the oxidation states of Ru and Ni, thereby modifying the electronic structures. As reported earlier, higher oxidation states of TMs in the layered structure are beneficial for OER [37]. Additionally, these higher oxidation states can be easily stabilized in DRX layered structures, which is essential for sustained OER [38]. Furthermore, it has also been widely accepted that high-valence transition metal cations facilitate the adsorption of OH− with the catalysts to form adsorbed −OOH species to promote OER reaction steps readily [8,39]. The above results reveal the enhanced electrochemical performance of **2** compared to not only **1** but also to many other cathode materials (Figure 3e).

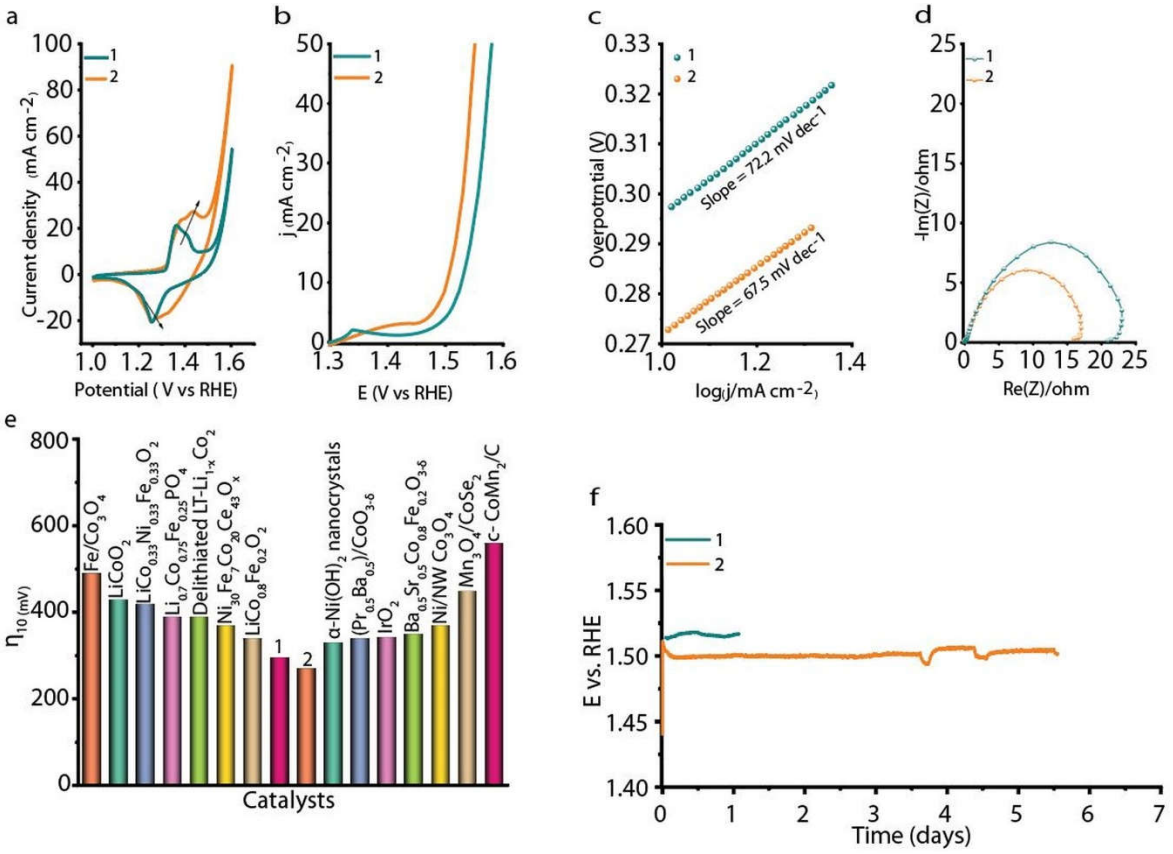

Figure 3. Comparison of electrochemical performances between **1** and **2**. (**a**) CV curves of **1** and **2** in oxygen saturated 1M KOH, where redox peaks indicate the electrochemical oxygen intercalation/(de)intercalation. (**b**) LSV Polarization curve of cathodes. (**c**) Tafel plots of cathodes, (**d**) Stability profiles, (**e**) Nyquist plots of cathodes in 1.0 M KOH, (**f**) Overpotentials at a standard current density of 10 mA cm^{-2}.

It is generally assumed that the oxygen BE at the surface largely influences the OER activity [8,40–42]. For this, we conducted a series of DFT calculations to investigate the role of Na-doping on surface oxygen atoms, as shown in Figure 4. The favorable locations of Ni and Na in **2** are found with Genetics Algorithm (GA). DFT calculations established that while Ni atoms prefer to occupy the Ru layer (Figure 4a), Na atoms prefer to locate in the Li layer (Figure 4b). Surprisingly, the average oxygen BEs in both cases are almost the same (~7 eV), but while it is almost uniform in **1**, **2** shows higher fluctuations. In particular, the lowest BE for oxygen is 5.45 eV in **2** and 6.51 eV in **1**. The Na-substitution promotes the OER activity by reducing the BE of some oxygen atoms at the surface and accentuating the facile diffusion of O_2 gas, which is consistent with experimental results. The total density of states (DOS) reveals that the electrons' occupancy near the Fermi level between **1** and **2** is different. In addition, the projected DOS of oxygen 2p orbital in **2** (Figure 4e) is substantially different from that in **1** (Figure 4d) and shows a shift in the O p-band center toward the Fermi level [43], which leads to better TM-O overlap and creates reduced charge transfer resistance well supported with Figure 3d.

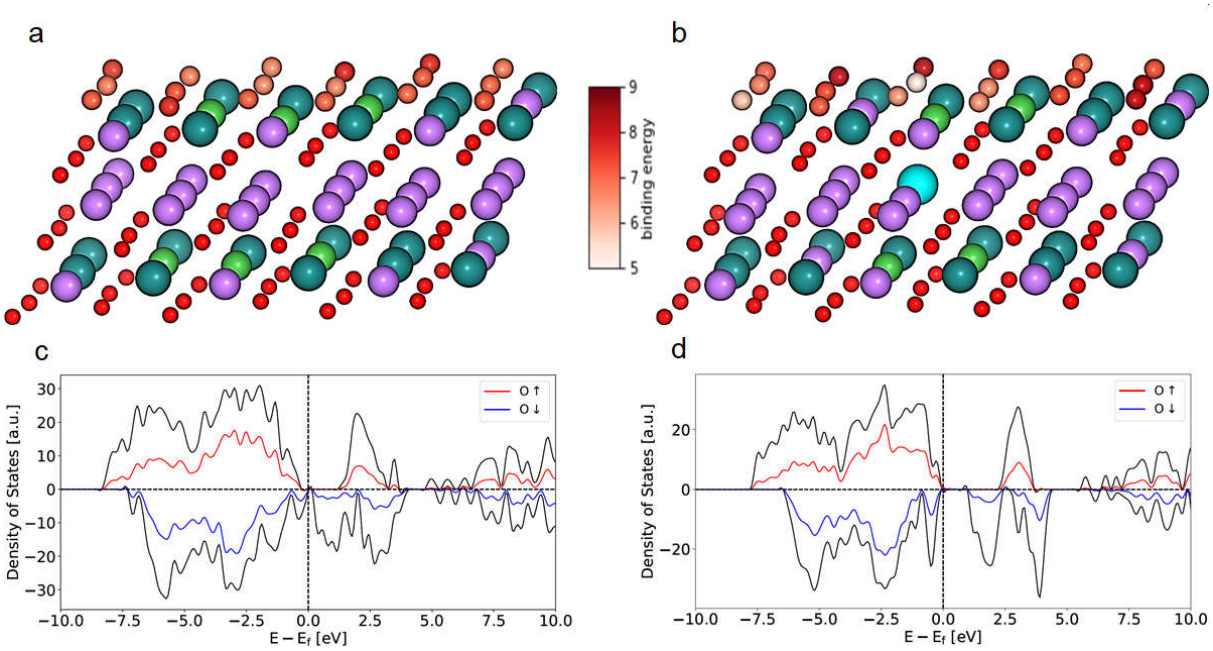

Figure 4. Effect of Na doping on the BE and projected DOS of O 2p of surface oxygen atoms. (**a**) **1**. (**b**) **2**. Atoms color code- O: red, Ru: dark green, Ni: light green, Na: light blue, Li: purple. The oxygen atoms at the top layer are shaded based on their binding energy. Total DOS (black line) and projected DOS (spin up: red line and spin down: blue line) of p orbitals of oxygen: (**c**) **1**. (**d**) **2**.

4. Summary and Conclusions

In summary, we have enrooted the idea of engaging cation-disordered cathode materials for OER application synthesized by a facile solid-state route. Na-doping in **2** solved the issue of instability prevailing in disordered cathodes but also contradicted the former idea that layered structures alone can stabilize TM oxidized species for improved OER performances. Nonetheless, **2** performs much better than **1** and many other layered cathode materials, including dedicated OER electrocatalysts. **2** requires a low η of 270/390 mV to display current densities of 10/250 mA cm^{-2} and demonstrate superior stability for more than 5.5 days, which is exceptionally better than many of the OER electrocatalysts reported to date. The significant enhancement in the OER performance is attributed to several interesting factors. First, the disordered structure provides better interaction between Li and TMs, often unavailable in layered cathodes where Li and TMs occupy a fixed position. Secondly, the induction of Na^+ promoted the oxidation state of TMs (Ni and Ru), favoring OER kinetics. Thirdly, DFT calculations predicted that Na^+ accentuates

the facile evolution of O_2 from the surface layer, thereby alleviating the sluggish reaction kinetics often observed in the OER. In addition, we are in the process of understanding the effect of Na doping to use this material as a battery material, and further works are in the pipeline to understand and explore the possibility of other doping sites (such as Ru or Li) and their influence on the electrochemical performances. We believe that our finding of engaging DRX cathode materials for the OER application will pave a novel design strategy for future materials of this family for high-performance electrocatalysts for energy conversion reactions.

Supplementary Materials: The following supporting information can be downloaded at: https://www.mdpi.com/article/10.3390/nano13010010/s1, Figure S1: Core-level XPS spectra of **1**. (a) Ni 2p. (b) Ru 3d. (c) O 1s.; Figure S2: Structural and elemental characterizations of **1**. (a) SEM image (scale bar 2 μm). (b) HRTEM image showing lattice fringe distance 0.258 nm corresponding to (002). (scale bar 2 nm). (c) the autocorrelated image corresponding to b. (d) High-angle annular dark-field scanning transmission electron microscopy (HAADF-STEM) and EDS elemental mapping of **1** (scale bar 250 nm); Figure S3: (a) Comparative LSV curves of **1**, **2**, and NF. (b) Plots of charging current density differences (Δj) vs. the scan rate for electrodes; Figure S4: Comparative LSV curves of **1**, **2**, and RuO_2; Figure S5: Cyclic voltammograms compared at different scan rate (a) **1**. (b) **2**; Figure S6: Equivalent circuit; Figure S7: HRTEM image after long-term stability (scale bar 2 nm). The lattice fringe distance after long-term stability remains almost same to that of Figure 2b; Figure S8: Calibration of the Hg/HgO reference electrode. For all measurements, Hg/HgO was used as the reference electrode. The Hg/HgO calibration with respect to the reversible hydrogen electrode (RHE) was performed in the high purity H_2 saturated electrolyte with Pt wire as the working electrode. LSV was run at a rate of 1 mV s^{-1}, and potential at zero mA current was taken to be the thermodynamic potential for hydrogen evolution reactions. So, in 1M KOH, E(RHE) = E(Hg/HgO) + 0.905; Table S1: The ICP-OES results of synthesized powders. The data shows the number of atoms per mole of material. The ICP-OES data were taken several times and the best data obtained are presented here with a round off to the nearest two decimal places. The data in parentheses () denotes the theoretical values; Table S2: A comparative chart for overpotential (η) of cathode materials used as OER electrocatalyst; S1. Effect of Na-doping on binding energy; S2. Structural characterizations. References [7, 9, 21, 23, 34, 44-64] are cited in the Supplementary Materials.

Author Contributions: Conceptualization, A.N.S. and K.-W.N.; methodology, A.N.S.; software, A.H. and M.H.; validation, A.M., A.N.S. and A.H.; formal analysis, H.-S.K.; investigation, A.N.S., A.H. and M.H.; resources, A.M.; data curation, A.N.S. and K.-W.N; writing—original draft preparation, A.N.S.; writing—review and editing, A.N.S., C.B., A.H. and K.-W.N.; visualization, A.M.; supervision, K.-W.N.; project administration, A.N.S.; funding acquisition, M.H. and K.-W.N. All authors have read and agreed to the published version of the manuscript.

Funding: This work was supported by the KISTI (KSC-2021-CRE-0193, KSC-2021-CRE-0195, KSC-2021-0367, KSC-2021-CRE-0519, KSC-2021-CRE-0554) and by the National Research Foundation of Korea (NRF) grant funded by the Korea government (MSIT, grant no. 2022M3J1A1054323).

Data Availability Statement: All the experimental data presented within this article, along with the supplementary information, will be made available from the authors upon reasonable request.

Acknowledgments: The author would like to thank Prof. K. S. Kim for his great support during the initial days of this project. Thanks also goes to Ms. Nivedita Singh for discussion on graphical abstract design.

Conflicts of Interest: The authors declare no conflict of interest.

References

1. Singh, A.N.; Kajal, S.; Kim, J.; Jana, A.; Kim, J.Y.; Kim, K.S. Interface Engineering Driven Stabilization of Halide Perovskites against Moisture, Heat, and Light for Optoelectronic Applications. *Adv. Energy Mater.* **2020**, *10*, 2000768. https://doi.org/10.1002/aenm.202000768.
2. Tiwari, J.N.; Singh, A.N.; Sultan, S.; Kim, K.S. Recent Advancement of p- and d-Block Elements, Single Atoms, and Graphene-Based Photoelectrochemical Electrodes for Water Splitting. *Adv. Energy Mater.* **2020**, *10*, 2000280. https://doi.org/10.1002/aenm.202000280.
3. Lewis, N.S.; Nocera, D.G. Powering the planet: Chemical challenges in solar energy utilization. *Proc. Natl. Acad. Sci. USA* **2006**, *103*, 15729–15735. https://doi.org/10.1073/pnas.0603395103.

4. Sultan, S.; Tiwari, J.N.; Singh, A.N.; Zhumagali, S.; Ha, M.; Myung, C.W.; Thangavel, P.; Kim, K.S. Single Atoms and Clusters Based Nanomaterials for Hydrogen Evolution, Oxygen Evolution Reactions, and Full Water Splitting. *Adv. Energy Mater.* **2019**, *9*, 1900624. https://doi.org/10.1002/aenm.201900624.
5. McCrory, C.C.L.; Jung, S.; Peters, J.C.; Jaramillo, T.F. Benchmarking Heterogeneous Electrocatalysts for the Oxygen Evolution Reaction. *J. Am. Chem. Soc.* **2013**, *135*, 16977–16987. https://doi.org/10.1021/ja407115p.
6. Zhu, Y.; Zhou, W.; Chen, Y.; Yu, J.; Liu, M.; Shao, Z. A High-Performance Electrocatalyst for Oxygen Evolution Reaction: $LiCo_{0.8}Fe_{0.2}O_2$. *Adv. Mater.* **2015**, *27*, 7150–7155. https://doi.org/10.1002/adma.201503532.
7. Lu, Z.; Wang, H.; Kong, D.; Yan, K.; Hsu, P.C.; Zheng, G.; Yao, H.; Liang, Z.; Sun, X.; Cui, Y. Electrochemical tuning of layered lithium transition metal oxides for improvement of oxygen evolution reaction. *Nat. Commun.* **2014**, *5*, 4345.
8. Zhu, K.; Wu, T.; Zhu, Y.; Li, X.; Li, M.; Lu, R.; Wang, J.; Zhu, X.; Yang, W. Layered Fe-Substituted $LiNiO_2$ Electrocatalysts for High-Efficiency Oxygen Evolution Reaction. *ACS Energy Lett.* **2017**, *2*, 1654–1660. https://doi.org/10.1021/acsenergylett.7b00434.
9. Zhu, Y.; Zhou, W.; Chen, Z.G.; Chen, Y.; Su, C.; Tadé, M.O.; Shao, Z. $SrNb_{0.1}Co_{0.7}Fe_{0.2}O_{3-\delta}$ perovskite as a next-generation electrocatalyst for oxygen evolution in alkaline solution. *Angew. Chem.* **2015**, *127*, 3969–3973.
10. Singh, A.N.; Kim, M.; Meena, A.; Wi, T.; Lee, H.; Kim, K.S. Na/Al Codoped Layered Cathode with Defects as Bifunctional Electrocatalyst for High-Performance Li-Ion Battery and Oxygen Evolution Reaction. *Small* **2021**, *17*, e2005605. https://doi.org/10.1002/smll.202005605.
11. Rosen, J.; Hutchings, G.S.; Jiao, F. Ordered Mesoporous Cobalt Oxide as Highly Efficient Oxygen Evolution Catalyst. *J. Am. Chem. Soc.* **2013**, *135*, 4516–4521. https://doi.org/10.1021/ja400555q.
12. Balasubramanian, M.; Melendres, C.A.; Mini, S. X-ray Absorption Spectroscopy Studies of the Local Atomic and Electronic Structure of Iron Incorporated into Electrodeposited Hydrous Nickel Oxide Films. *J. Phys. Chem. B* **2000**, *104*, 4300–4306. https://doi.org/10.1021/jp9921710.
13. Tong, Y.; Guo, Y.; Chen, P.; Liu, H.; Zhang, M.; Zhang, L.; Yan, W.; Chu, W.; Wu, C.; Xie, Y. Spin-State Regulation of Perovskite Cobaltite to Realize Enhanced Oxygen Evolution Activity. *Chem* **2017**, *3*, 812–821. https://doi.org/10.1016/j.chempr.2017.09.003.
14. Delmas, C.; Croguennec, L. Layered Li (Ni, M)O_2 systems as the cathode material in lithium-ion batteries. *MRS Bull.* **2002**, *27*, 608–612.
15. Prado, G.; Fournes, L.; Delmas, C. On the LixNi0.70Fe0.15$Co_{0.15}O_2$ system: An X-ray diffraction and Mössbauer study. *J. Solid State Chem.* **2001**, *159*, 103–112.
16. Singh, A.N. A Story of Disordered Arrangements. *Matter* **2021**, *4*, 23–25. https://doi.org/10.1016/j.matt.2020.12.021.
17. Kresse, G.; Furthmüller, J. Efficient iterative schemes for ab initio total-energy calculations using a plane-wave basis set. *Phys. Rev. B* **1996**, *54*, 11169.
18. Blöchl, P.E. Projector augmented-wave method. *Phys. Rev. B Condens. Matter Mater. Phys.***1994**, *50*, 17953–17979. https://doi.org/10.1103/PhysRevB.50.17953.
19. Perdew, J.P.; Ernzerhof, M.; Burke, K. Rationale for mixing exact exchange with density functional approximations. *J. Chem. Phys.* **1996**, *105*, 9982–9985. htttps://doi:10.1063/1.472933.
20. Hajibabaei, A.; Myung, C.W.; Kim, K.S. Sparse Gaussian process potentials: Application to lithium diffusivity in superionic conducting solid electrolytes. *Phys. Rev. B* **2021**, *103*, 214102. https://doi.org/10.1103/physrevb.103.214102.
21. Hajibabaei, A.; Kim, K.S. Universal Machine Learning Interatomic Potentials: Surveying Solid Electrolytes. *J. Phys. Chem. Lett.* **2021**, *12*, 8115–8120. https://doi.org/10.1021/acs.jpclett.1c01605.
22. Hajibabaei, A.; Ha, M.; Pourasad, S.; Kim, J.; Kim, K.S. Machine Learning of First-Principles Force-Fields for Alkane and Polyene Hydrocarbons. *J. Phys. Chem. A* **2021**, *125*, 9414–9420. https://doi.org/10.1021/acs.jpca.1c05819.
23. Miura, Y.; Yasui, Y.; Sato, M.; Igawa, N.; Kakurai, K. New-type phase transition of Li2RuO3 with honeycomb structure. *J. Phys. Soc. Jpn.* **2007**, *76*, 033705.
24. Xu, J.; Sun, M.; Qiao, R.; Renfrew, S.; Ma, L.; Wu, T.; Hwang, S.; Nordlund, D.; Su, D.; Amine, K.; et al. Elucidating anionic oxygen activity in lithium-rich layered oxides. *Nat. Commun.* **2018**, *9*, 947. https://doi.org/10.1038/s41467-018-03403-9.
25. Lee, J.; Urban, A.; Li, X.; Su, D.; Hautier, G.; Ceder, G. Unlocking the Potential of Cation-Disordered Oxides for Rechargeable Lithium Batteries. *Science* **2014**, *343*, 519–522. https://doi.org/10.1126/science.1246432.
26. Al-Tabbakh, A.A.; Karatepe, N.; Al-Zubaidi, A.B.; Benchaabane, A.; Mahmood, N.B. Crystallite size and lattice strain of lithiated spinel material for rechargeable battery by X-ray diffraction peak-broadening analysis. *Int. J. Energy Res.* **2019**, *43*, 1903–1911. https://doi.org/10.1002/er.4390.
27. Jiang, H.; Gu, J.; Zheng, X.; Liu, M.; Qiu, X.; Wang, L.; Li, W.; Chen, Z.; Ji, X.; Li, J. Defect-rich and ultrathin N doped carbon nanosheets as advanced trifunctional metal-free electrocatalysts for the ORR, OER and HER. *Energy Environ. Sci.* **2018**, *12*, 322–333. https://doi.org/10.1039/c8ee03276a.
28. Fabbri, E.; Habereder, A.; Waltar, K.; Kötz, R.; Schmidt, T.J. Developments and perspectives of oxide-based catalysts for the oxygen evolution reaction. *Catal. Sci. Technol.* **2014**, *4*, 3800–3821. https://doi.org/10.1039/c4cy00669k.
29. Paoli, E.A.; Masini, F.; Frydendal, R.; Deiana, D.; Schlaup, C.; Malizia, M.; Hansen, T.W.; Horch, S.; Stephens, I.E.L.; Chorkendorff, I. Oxygen evolution on well-characterized mass-selected Ru and RuO_2nanoparticles. *Chem. Sci.* **2014**, *6*, 190–196. https://doi.org/10.1039/c4sc02685c.

30. Pan, Y.; Xu, X.; Zhong, Y.; Ge, L.; Chen, Y.; Veder, J.-P.M.; Guan, D.; O'Hayre, R.; Li, M.; Wang, G.; et al. Direct evidence of boosted oxygen evolution over perovskite by enhanced lattice oxygen participation. *Nat. Commun.* **2020**, *11*, 2002. https://doi.org/10.1038/s41467-020-15873-x.
31. Liu, R.; Liang, F.; Zhou, W.; Yang, Y.; Zhu, Z. Calcium-doped lanthanum nickelate layered perovskite and nickel oxide nano-hybrid for highly efficient water oxidation. *Nano Energy* **2015**, *12*, 115–122. https://doi.org/10.1016/j.nanoen.2014.12.025.
32. Liang, F.; Yu, Y.; Zhou, W.; Xu, X.; Zhu, Z. Highly defective CeO_2 as a promoter for efficient and stable water oxidation. *J. Mater. Chem. A* **2014**, *3*, 634–640. https://doi.org/10.1039/c4ta05770h.
33. Lv, Z.; Zhang, Y.; Wang, K.; Yu, T.; Liu, X.; Wang, G.; Xie, G.; Jiang, L. High performance of Co–P/NF electrocatalyst for oxygen evolution reaction. *Mater. Chem. Phys.* **2019**, *235*, 121772. https://doi.org/10.1016/j.matchemphys.2019.121772.
34. Tian, Z.; Wang, J.; Liu, S.; Li, Q.; Zeng, G.; Yang, Y.; Cui, Y. Na-stabilized Ru-based lithium rich layered oxides with enhanced electrochemical performance for lithium ion batteries. *Electrochim. Acta* **2017**, *253*, 31–38. https://doi.org/10.1016/j.electacta.2017.09.032.
35. Min, H.; Kim, M.; Lee, S.U.; Kim, H.; Kim, G.; Choi, K.; Lee, J.H.; Seok, S.I. Efficient, stable solar cells by using inherent bandgap of α-phase formamidinium lead iodide. *Science* **2019**, *366*, 749–753.
36. Jia, Y.; Zhang, L.; Du, A.; Gao, G.; Chen, J.; Yan, X.; Brown, C.L.; Yao, X. Defect Graphene as a Trifunctional Catalyst for Electrochemical Reactions. *Adv. Mater.* **2016**, *28*, 9532–9538. https://doi.org/10.1002/adma.201602912.
37. Delmas, C.; Prado, G.; Rougier, A.; Suard, E.; Fournes, L. Effect of iron on the electrochemical behaviour of lithium nickelate: From $LiNiO_2$ to 2D-$LiFeO_2$. *Solid State Ion.* **2000**, *135*, 71–79.
38. Prado, G.; Rougier, A.; Fournès, L.; Delmas, C. Electrochemical Behavior of Iron-Substituted Lithium Nickelate. *J. Electrochem. Soc.* **2000**, *147*, 2880–2887. https://doi.org/10.1149/1.1393620.
39. Mansour, A.N.; Yang, X.Q.; Sun, X.; McBreen, J.; Croguennec, L.; Delmas, C. In Situ X-Ray Absorption Spectroscopy Study of Li (1− z) Ni (1+ z) O 2 (z≤ 0.02) Cathode Material. *J. Electrochem. Soc.* **2000**, *147*, 2104.
40. Stamenkovic, V.R.; Strmcnik, D.; Lopes, P.; Markovic, V.R.S.D.S.P.P.L.N.M. Energy and fuels from electrochemical interfaces. *Nat. Mater.* **2016**, *16*, 57–69. https://doi.org/10.1038/nmat4738.
41. Rossmeisl, J.; Qu, Z.-W.; Zhu, H.; Kroes, G.-J.; Nørskov, J.K. Electrolysis of water on oxide surfaces. *J. Electroanal. Chem.* **2007**, *607*, 83–89. https://doi.org/10.1016/j.jelechem.2006.11.008.
42. Over, H. Surface chemistry of ruthenium dioxide in heterogeneous catalysis and electrocatalysis: From fundamental to ap-plied research. *Chem. Rev.* **2012**, *112*, 3356–3426.
43. Liu, Z.; Sun, Y.; Wu, X.; Hou, C.; Geng, Z.; Wu, J.; Huang, K.; Gao, L.; Feng, S. Charge transfer-induced O p-band center shift for an enhanced OER performance in $LaCoO_3$ film. *CrystEngComm* **2019**, *21*, 1534–1538. https://doi.org/10.1039/c8ce01849a.
44. Gershinsky, Y.; Zitoun, D. Direct Chemical Synthesis of Lithium Sub-Stochiometric Olivine $Li_{0.7}Co_{0.75}Fe_{0.25}PO_4$ Coated with Reduced Graphene Oxide as Oxygen Evolution Reaction Electrocatalyst. *ACS Catal*. **2018**, *8*, 8715–8725.
45. Haber, J.A.; Cai, Y.; Jung, S.; Xiang, C.; Mitrovic, S.; Jin, J.; Bell, A.T.; Gregoire, J.M. Discovering Ce-rich oxygen evolution catalysts, from high throughput screening to water electrolysis. *Energy Environ. Sci.* **2014**, *7*, 682–688. https://doi.org/10.1039/c3ee43683g.
46. Trotochaud, L.; Ranney, J.K.; Williams, K.N.; Boettcher, S.W. Solution-Cast Metal Oxide Thin Film Electrocatalysts for Oxygen Evolution. *J. Am. Chem. Soc.* **2012**, *134*, 17253–17261. https://doi.org/10.1021/ja307507a.
47. Liang, H.; Meng, F.; Cabán-Acevedo, M.; Li, L.; Forticaux, A.; Xiu, L.; Wang, Z.; Jin, S. Hydrothermal continuous flow synthesis and exfoliation of NiCo layered double hydroxide nanosheets for enhanced oxygen evolution catalysis. *Nano Lett.* **2015**, *15*, 1421–1427.
48. Peng, X.; Wang, L.; Hu, L.; Li, Y.; Gao, B.; Song, H.; Huang, C.; Zhang, X.; Fu, J.; Huo, K.; et al. In situ segregation of cobalt nanoparticles on VN nanosheets via nitriding of $Co_2V_2O_7$ nanosheets as efficient oxygen evolution reaction electrocatalysts. *Nano Energy* **2017**, *34*, 1–7. https://doi.org/10.1016/j.nanoen.2017.02.016.
49. Li, C.; Han, X.; Cheng, F.; Hu, Y.; Chen, C.; Chen, J. Phase and composition controllable synthesis of cobalt manganese spinel nanoparticles towards efficient oxygen electrocatalysis. *Nat. Commun.* **2015**, *6*, 7345. https://doi.org/10.1038/ncomms8345.
50. Bao, J.; Zhang, X.; Fan, B.; Zhang, J.; Zhou, M.; Yang, W.; Hu, X.; Wang, H.; Pan, B.; Xie, Y. Ultrathin Spinel-Structured Nanosheets Rich in Oxygen Deficiencies for Enhanced Electrocatalytic Water Oxidation. *Angew. Chem.* **2015**, *127*, 7507–7512. https://doi.org/10.1002/ange.201502226.
51. Lu, Z.; Xu, W.; Zhu, W.; Yang, Q.; Lei, X.; Liu, J.; Li, Y.; Sun, X.; Duan, X. Three-dimensional NiFe layered double hydroxide film for high-efficiency oxygen evolution reaction. *Chem. Commun.* **2014**, *50*, 6479–6482. https://doi.org/10.1039/c4cc01625d.
52. Suntivich, J.; May, K.J.; Gasteiger, H.A.; Goodenough, J.B.; Shao-Horn, Y. A perovskite oxide optimized for oxygen evolu-tion catalysis from molecular orbital principles. *Science* **2011**, *334*, 1383–1385.
53. Fan, K.; Chen, H.; Ji, Y.; Huang, H.; Claesson, H.H.P.M.; Daniel, Q.; Philippe, B.; Rensmo, B.P.H.; Li, F.; Luo, Y.; et al. Nickel–vanadium monolayer double hydroxide for efficient electrochemical water oxidation. *Nat. Commun.* **2016**, *7*, 11981. https://doi.org/10.1038/ncomms11981.
54. Zhang, Y.; Wang, X.; Luo, F.; Tan, Y.; Zeng, L.; Fang, B.; Liu, A. Rock salt type $NiCo_2O_3$ supported on ordered mesoporous carbon as a highly efficient electrocatalyst for oxygen evolution reaction. *Appl. Catal. B Environ.* **2019**, *256*, 117852. https://doi.org/10.1016/j.apcatb.2019.117852.

55. Indra, A.; Menezes, P.W.; Sahraie, N.R.; Bergmann, A.; Das, C.; Tallarida, M.; Schmeißer, D.; Strasser, P.; Driess, M. Unifica-tion of catalytic water oxidation and oxygen reduction reactions: Amorphous beat crystalline cobalt iron oxides. *J. Am. Chem. Soc.* **2014**, *136*, 17530–17536.
56. Chakrapani, K.; Bendt, G.; Hajiyani, H.; Lunkenbein, T.; Greiner, M.T.; Masliuk, L.; Salamon, S.; Landers, J.; Schloegl, R.; Wende, H.; et al. The Role of Composition of Uniform and Highly Dispersed Cobalt Vanadium Iron Spinel Nanocrystals for Oxygen Electrocatalysis. *ACS Catal.* **2018**, *8*, 1259–1267. https://doi.org/10.1021/acscatal.7b03529.
57. Li, M.; Zhu, Y.; Wang, H.; Wang, C.; Pinna, N.; Lu, X. Ni Strongly Coupled with Mo_2C Encapsulated in Nitrogen-Doped Carbon Nanofibers as Robust Bifunctional Catalyst for Overall Water Splitting. *Adv. Energy Mater.* **2019**, *9*, 1803185. https://doi.org/10.1002/aenm.201803185.
58. Grimaud, A.; May, K.J.; Carlton, C.E.; Lee, Y.-L.; Risch, M.; Hong, W.T.; Zhou, J.; Shao-Horn, Y. Double perovskites as a family of highly active catalysts for oxygen evolution in alkaline solution. *Nat. Commun.* **2013**, *4*, 2439. https://doi.org/10.1038/ncomms3439.
59. Liu, H.; He, Q.; Jiang, H.; Lin, Y.; Zhang, Y.; Habib, M.; Chen, S.; Song, L. Electronic Structure Reconfiguration toward Pyrite NiS_2 via Engineered Heteroatom Defect Boosting Overall Water Splitting. *ACS Nano* **2017**, *11*, 11574–11583. https://doi.org/10.1021/acsnano.7b06501.
60. Fan, K.; Zou, H.; Lu, Y.; Chen, H.; Li, F.; Liu, J.; Sun, L.; Tong, L.; Toney, M.F.; Sui, M.; et al. Direct Observation of Structural Evolution of Metal Chalcogenide in Electrocatalytic Water Oxidation. *ACS Nano* **2018**, *12*, 12369–12379. https://doi.org/10.1021/acsnano.8b06312.
61. Tiwari, J.N.; Dang, N.K.; Sultan, S.; Thangavel, P.; Jeong, H.Y.; Kim, K.S. Multi-heteroatom-doped carbon from waste-yeast biomass for sustained water splitting. *Nat. Sustain.* **2020**, *3*, 556–563. https://doi.org/10.1038/s41893-020-0509-6.
62. Qu, M.; Ding, X.; Shen, Z.; Cui, M.; Oropeza, F.E.; Gorni, G.; O'Shea, V.A.D.L.P.; Li, W.; Qi, D.-C.; Zhang, K.H.L. Tailoring the Electronic Structures of the La_2NiMnO_6 Double Perovskite as Efficient Bifunctional Oxygen Electrocatalysis. *Chem. Mater.* **2021**, *33*, 2062–2071. https://doi.org/10.1021/acs.chemmater.0c04527.
63. Baumung, M.; Schönewald, F.; Erichsen, T.; Volkert, C.A.; Risch, M. Influence of particle size on the apparent electrocatalytic activity of $LiMn_2O_4$ for oxygen evolution. *Sustain. Energy Fuels* **2019**, *3*, 2218–2226. https://doi.org/10.1039/c8se00551f.
64. Wang, H.; Liang, Z.; Tang, M.; Chen, G.; Li, Y.; Chen, W.; Lin, D.; Zhang, Z.; Zhou, G.; Li, J.; et al. Self-Selective Catalyst Synthesis for CO_2 Reduction. *Joule* **2019**, *3*, 1927–1936. https://doi.org/10.1016/j.joule.2019.05.023.